
Research Article: New Research / Neuronal Excitability

Precision Mapping of Amyloid- β Binding Reveals Perisynaptic Localization and Spatially Restricted Plasticity Deficits

<https://doi.org/10.1523/ENEURO.0416-21.2021>

Cite as: eNeuro 2021; 10.1523/ENEURO.0416-21.2021

Received: 4 October 2021

Revised: 3 November 2021

Accepted: 11 November 2021

This Early Release article has been peer-reviewed and accepted, but has not been through the composition and copyediting processes. The final version may differ slightly in style or formatting and will contain links to any extended data.

Alerts: Sign up at www.eneuro.org/alerts to receive customized email alerts when the fully formatted version of this article is published.

Copyright © 2021 Actor-Engel et al.

This is an open-access article distributed under the terms of the Creative Commons Attribution 4.0 International license, which permits unrestricted use, distribution and reproduction in any medium provided that the original work is properly attributed.

1
2
3
4
5

6 **Precision mapping of amyloid beta binding reveals perisynaptic localization and**
7 **spatially restricted plasticity deficits**

8
9
10
11
12
13
14
15
16

17 Hannah S. Actor-Engel¹, Samantha L. Schwartz¹, Kevin C. Crosby¹, Brooke L. Sinnen¹,
18 Olga Prikhodko¹, Harrison J. Ramsay¹, Jennifer N. Bourne, Christina S. Winborn¹,
19 Alexandra Lucas¹, Katherine R. Smith¹, Mark L. Dell'Acqua¹, Matthew J. Kennedy^{1*}

20

21

22 ¹Department of Pharmacology, University of Colorado School of Medicine, Anschutz
23 Medical Campus, Aurora CO 80045

24

25

*Correspondence: matthew.kennedy@cuanschutz.edu

26

27

28 # Pages: 46

29 # Figures: 5 main, plus 1 Extended Data

30 # Words

31 Abstract: 192

32 Introduction: 512

33 Discussion: 838

34

35 **Acknowledgements:** The authors wish to thank Chandra Tucker for critical discussions
36 in preparing this manuscript. We would also like to acknowledge the University of
37 Colorado Advanced Light Microscopy Core Facility. The work was supported by
38 National Institute of Neurological Disorders and Stroke R35NS116879 (M.J.K.);
39 NS110383 (M.J.K., M.L.D.); National Institute on Aging T32AG000279 (H.S.A.);
40 AG058005 (M.J.K.) and National Institute of Mental Health R01MH119154 (K.R.S.).

41

42

43 The authors declare no competing conflicts of interest

44

45

46

47 **Abstract**

48

49 Secreted beta amyloid (A β) peptide forms neurotoxic oligomeric assemblies thought to
50 cause synaptic deficits associated with Alzheimer's disease. Soluble A β oligomers
51 (A β o) directly bind to neurons with high affinity and block plasticity mechanisms related
52 to learning and memory, trigger loss of excitatory synapses and eventually cause cell
53 death. While A β o toxicity has been intensely investigated, it remains unclear precisely
54 where A β o initially binds to the surface of neurons and whether sites of binding relate to
55 synaptic deficits. Here we used a combination of live cell, super resolution and
56 ultrastructural imaging techniques to investigate the kinetics, reversibility and nanoscale
57 location of A β o binding. Surprisingly, A β o does not bind directly at the synaptic cleft as
58 previously thought, but instead forms distinct nanoscale clusters encircling the
59 postsynaptic membrane with a significant fraction also binding presynaptic axon
60 terminals. Synaptic plasticity deficits were observed at A β o-bound synapses but not
61 closely neighboring A β o-free synapses. Thus, perisynaptic A β o binding triggers spatially
62 restricted signaling mechanisms to disrupt synaptic function. These data provide new
63 insight into the earliest steps of A β o pathology and lay the groundwork for future studies
64 evaluating potential surface receptor(s) and local signaling mechanisms responsible for
65 A β o binding and synapse dysfunction.

66

67 **Significance Statement:** Amyloid beta (A β) is one of the principal neurotoxic agents
68 responsible for Alzheimer's disease. Defining where A β attaches to neurons is critical
69 for understanding its toxicity and role in disease. Here we used high resolution
70 microscopy techniques to demonstrate A β rapidly forms stable nanoscale clusters
71 immediately adjacent to a subset of excitatory synaptic connections. Synaptic plasticity
72 was only impaired at A β -targeted synapses and not at neighboring A β -free synapses.
73 Thus, perisynaptic A β binding rapidly triggers locally restricted signaling mechanisms
74 underlying its synaptic toxicity.
75

76 **Introduction**

77 Amyloid beta (A β) is widely recognized as a primary neuropathologic agent in
78 Alzheimer's disease (AD). Formed by proteolytic processing of amyloid precursor
79 protein (APP), A β peptide self-associates to form soluble oligomers and fibrils before
80 eventually depositing into the hallmark plaques associated with AD (Gong et al., 2003;
81 Lambert et al., 1998; Lesne et al., 2006; Seubert et al., 1992; Shoji et al., 1992). While
82 A β plaques correlate with neuronal dysfunction and cell death, considerable evidence
83 supports a major role for soluble, oligomeric A β (A β o) in synapse toxicity. For example,
84 synapse loss and memory impairment in AD can occur prior to widespread plaque
85 formation (Dekosky, 1990; Terry et al., 1991). Acute exposure to nano- to picomolar
86 quantities of A β o, either *in vivo* or *in vitro*, is sufficient to block neural plasticity within
87 minutes, trigger synapse elimination over days, and eventually cause cell death
88 (Shankar et al., 2007; Shankar et al., 2008; Sinnen et al., 2016; Walsh, 2002; Wei et al.,
89 2010).

90 Pioneering studies demonstrated A β o preferentially accumulates at excitatory
91 synapses within minutes following application of synthetic "amyloid- β derived diffusible
92 ligands" (ADDLs) (Koffie et al., 2009; Lacor et al., 2004; Renner et al., 2010). Consistent
93 with these studies, naturally derived A β produced over much longer timescales
94 (months/years) also accumulates at synaptic sites in both animal AD models and
95 human AD patients (Games et al., 1995; Gong et al., 2003; Koffie et al., 2009; Pickett et
96 al., 2016). While these observations suggest a direct role of A β in synapse toxicity, little
97 is known about the earliest steps of A β o binding. Precisely where does A β o engage
98 neurons relative to synaptic connections? Does it bind to pre- or postsynaptic

99 compartments? How fast does it associate and dissociate? Are only A β o-bound
100 synapses impaired? Addressing these questions will be important for understanding the
101 mechanisms of A β o toxicity. For example, mapping where A β o binds to neurons with
102 nanometer precision will be imperative for evaluating putative A β o receptors. Thus far,
103 over 20 A β receptors have been described, each with diverse subcellular localizations,
104 including the presynaptic membrane, the postsynaptic membrane, peri- and non-
105 synaptic sites, yet whether A β o directly binds at these sites remains unclear.
106 Furthermore, whether A β o binding triggers cell wide synaptic dysfunction or selectively
107 impairs synapses to which it is bound is not known.

108 Using longitudinal live imaging, we demonstrate acutely applied A β o rapidly
109 forms stable clusters on the neuronal cell surface. In agreement with previous studies,
110 A β o preferentially associates with excitatory synapses. However, super resolution light
111 microscopy, immunogold electron microscopy, and expansion microscopy revealed that
112 A β o does not bind directly at the synaptic cleft, but instead forms stable nanoscale
113 clusters encircling the postsynaptic membrane with a significant fraction also binding the
114 presynaptic axon terminal. Finally, we used 2-photon glutamate uncaging at individual
115 synapses to demonstrate plasticity deficits are restricted to A β o-bound spines. Together
116 these results provide the first quantitative, super-resolution interrogation of the earliest
117 steps of A β o binding, dynamics and local toxicity at synaptic sites. Defining precisely
118 where A β o initially engages the neuronal surface is a key step in understanding how
119 A β o causes synaptic dysfunction and for directing future strategies aimed at preventing
120 A β o-induced pathology.

121

122 **Materials and Methods**

123 *Cell Culture and transfection*

124 All animal procedures were carried out in accordance with the Institutional Animal Care
125 and Use Committee at the University of Colorado, Anschutz Medical Campus. Primary
126 hippocampal cultures were made from P0-P1 Sprague Dawley rats as previously
127 described (Sinnen et al., 2016) and maintained in Neurobasal media (Gibco) with B27
128 supplement (Gibco) for 15-18 days in vitro (DIV) prior to experiments. Neurons were
129 typically transfected between DIV 15 and 17 using lipofectamine 2000 according to the
130 manufacturer's instructions. Plasmids used in this study include: PSD95_{FingR}-GFP (Gift
131 from Dr. Don Arnold, University of Southern California) and pCAG-mCh, pCAG-GFP
132 and pSyn-tdtomato plasmids (where pCAG is the chick β-actin promoter; pSyn is human
133 synapsin promoter).

134

135 *Aβ Preparation*

136 Soluble Aβ1-42 (Anaspec) oligomers were prepared similar to a previously reported
137 method (Klein, 2002). Briefly, Aβ was dissolved in 1,1,1,3,3,3-Hexafluoro-2-propanol,
138 aliquoted and dried in a chemical fume hood and stored at -80. The day before use, Aβ
139 (6nmol) was dissolved in 4μL of dimethyl sulfoxide and then 60μL of phosphate buffered
140 saline (PBS) was added for a final concentration of 94 μM. The dissolved peptide was
141 incubated at 4°C overnight. Following 12-24h incubation, the sample was centrifuged at
142 14,000 xg at 4°C. The supernatant was reserved and applied to a size exclusion spin
143 filter (30KD cutoff; millipore, MRCFOR030) and centrifuged for 10 min at 10,000 xg at

144 room temperature to remove low molecular weight A β species. The high molecular
145 weight fraction was diluted to a final volume of 600 μ l with PBS (working concentration
146 of 10 μ M) and stored on ice until use. For experiments using fluorescent A β o, the
147 preparation was carried out as described above with HiLyte647-conjugated A β
148 (Anaspec) included at a molar ratio of 1:3, labeled:unlabeled A β peptide.

149

150 *Live-cell imaging*

151 Live-cell imaging of dissociated neurons was performed at 31°C on an Olympus IX71
152 equipped with a spinning-disc scan head (Yokogawa). Excitation illumination was
153 delivered from an acousto-optic tunable filter (AOTF) controlled laser launch (Andor).
154 Images were acquired using a 60x Plan Apochromat 1.4 numerical aperture objective
155 and collected on a 1024 X 1024 pixel Andor iXon EM-CCD camera. Data acquisition
156 and analysis were performed with MetaMorph (Molecular Devices), Andor IQ, and
157 ImageJ software.

158 For live cell A β o binding experiments, z-stacks were acquired every 10 s.
159 Labeled A β was added to the imaging chamber following a baseline acquisition imaging
160 period. For A β o dissociation experiments, A β o was added to the imaging chamber and
161 allowed to bind for 10 min. The imaging media was then exchanged by washing 3x with
162 A β o-free media. Synapse-associated A β o was quantified by creating a binary mask
163 based on the PSD95 signal and then calculating the average, background-subtracted
164 integrated density. Extrasynaptic A β o was quantified within a mask created by
165 subtracting the PSD95 mask from a cell fill mask. Binding kinetics were calculated by

166 fitting plots of the A β o fluorescent signal (F/F_0) vs time with a single exponential
167 function.

168

169 *Fluorescence Recovery after Photobleaching (FRAP)*

170 A β o was added to coverslips for at least 10 min to allow binding to saturate. Baseline
171 images were acquired once every 15 s for 12 frames. A β o puncta were bleached using
172 galvanometric mirrors (FRAPPA module, Andor technologies) to steer a diffraction
173 limited excitation spot over the region of interest. Photobleaching was typically carried
174 out using 60% laser power from a fiber-coupled 100mW 641 laser with a dwell time of
175 1 msec. Following photobleaching, images were acquired at 1 frame/min for 25 min.

176

177 *Structural LTP/2-photon glutamate uncaging*

178 2-photon glutamate uncaging and imaging were carried out using a Bruker Optima laser
179 scanning microscope equipped with a Mai-Tai DeepSee laser (Spectra-Physics) for
180 imaging and a Mai-tai laser (Spectra-Physics) for uncaging. Hippocampal neurons
181 transfected with GFP or tdTomato expressing plasmids were treated with A β o
182 generated with either HiLyte568 or HiLyte488-labeled A β peptide respectively. Full z-
183 stacks were acquired to identify A β o-bound spines using sequential 920/1040nm
184 excitation (GFP/HiLyte568) or single 920nm excitation (tdTom/HiLyte488 A β o). A β o-
185 positive and negative spines were subject to glutamate uncaging in ACSF containing 3
186 mM Ca²⁺ and lacking Mg²⁺. Uncaging power and duration were calibrated so that
187 dendritic spine Ca²⁺ influx triggered by glutamate uncaging (measured in separate cells
188 expressing GCaMP6) matched Ca²⁺ influx resulting from spontaneous glutamate

189 release (Sinnen et al., 2016). Spine growth was triggered by MNi-glutamate (2mM)
190 uncaging at 720 nm with a train of 45 1 msec pulses delivered at 0.5 Hz at a single spot
191 adjacent to the tip of the targeted spine. A mix of A β -positive and negative spines were
192 selected from each cell. Z-stacks were acquired every 90 sec to visualize spine
193 morphology pre- and post-glutamate uncaging.

194

195 *Immunocytochemistry*

196 Cultured neurons were fixed with 4% PFA for 10 min at room temperature,
197 permeabilized with 0.1% triton for 10 min, and blocked with 5% BSA in PBS for 30min.
198 Primary antibodies were diluted with PBS containing 3% BSA and added to fixed cells
199 for 2hr at room temperature. Anti- β -Amyloid 1-16 Biolegend 6E10, Cat# 803014
200 (1:1000); PSD95, Millipore Cat#: MAB1596 (1:1000); GluA1- Polyclonal (1:300) (Hiester
201 et al., 2017; Kennedy et al., 2010); Gephyrin, Synaptic systems Cat# 147011 (1:1000);
202 Bassoon, Synaptic Systems Cat# 141004 (1:1000). Cells were washed with PBS in
203 between primary and secondary incubations. Samples were incubated with
204 fluorescently conjugated secondary antibodies (1:2000) for 1hr at room temperature.

205

206 *Structured Illumination Microscopy (SIM)*

207 Multichannel SIM images of A β -treated neurons were acquired with a Nikon N-SIM E
208 structured illumination microscope using a 100x 1.49 NA objective, and reconstructed
209 using Nikon Elements software as described previously with minor modifications
210 (Crosby et al., 2019; Smith et al., 2014). Imaging parameters (laser power, exposure)
211 were optimized for a high signal to noise ratio (>8). For each coverslip imaged, the

212 objective correction collar was adjusted automatically and a fourier transform image was
213 used to confirm optimal correction collar adjustment. Z-stacks ($z=0.2 \mu\text{m}$, 13 slices)
214 were reconstructed using Nikon Elements software. For 3D stack reconstruction, the
215 illumination modulation contrast was set automatically and the high-resolution noise
216 suppression was set to 1, and kept consistent across all images.

217

218 *SIM Analysis*

219 Quantification of A β density distribution relative to specific proteins of interest was
220 performed using custom analysis software written in Matlab along with the freely
221 available Matlab Toolbox DiplImage (Delft). Proteins of interest were identified as
222 follows. Each channel of the image was smoothed using a Laplacian or Gaussian filter
223 to enhance punctate objects with a kernel size of 2 pixels in X and Y and 1 pixel in Z. An
224 automatic intensity threshold was calculated using the Matlab “multithresh” function to
225 identify two threshold levels based on the image intensity histogram. The higher
226 threshold was used to generate a mask for each image. The DiplImage ‘label’ function
227 was then used to identify individual objects from the mask and then a 3-dimensional
228 (3D) Euclidean distance transform was applied using the Matlab function ‘bwdistc1.m’
229 DOI: 10.1007/s11760-012-0419-9, resulting in a new distance image in which each
230 voxel of the image represents the 3D distance to the closest masked object. To mask
231 the A β signal a similar process was used, however, because the A β puncta were more
232 densely spaced, an additional watershed filter was used to improve segmentation.
233 Watershed lines were computed from the gaussian filtered ($s_{xy} = 1$) original image with
234 a connectivity of 1 pixel on a frame-to-frame basis using the DiplImage ‘gaussf’ and

235 ‘watershed’ functions and then subtracted from the A β mask. The center of mass
236 positions for each labeled A β puncta were next identified using the DiplImage ‘measure’
237 function. The distance image could then be used to identify the shell of voxels within a
238 specified distance from the proteins of interest. The count of A β puncta center positions
239 within this volume of voxels approximates the A β density within the specified distance
240 range. Resulting densities were then divided by a normalization term representing the
241 expected density from a uniform A β distribution, such that values >1 represent an A β
242 density above uniform. To generate this normalization term, a simulation for each image
243 was performed by randomly distributing the same number of A β puncta found in the
244 original image within 642 nm (20 * X-Y pixel size) of the proteins of interest and then
245 calculating the density within each distance range. To prevent any artifact arising from
246 the difference in Z pixel size compared to X-Y pixel size in SIM images, the number of
247 A β puncta at each z plane was kept the same between the original image and the
248 simulated image.

249

250 *Direct Stochastic Reconstruction Microscopy (dSTORM) imaging and analysis*

251 Cells exposed to 500nM A β o-647 for 10 min or anti-GluA1 for 15 min were fixed and
252 labeled with anti-PSD95 as described above. Secondary antibodies were conjugated to
253 either Alexa647 or CF568. Following secondary antibody labeling, cells were post-fixed
254 with 4% paraformaldehyde for 15 min. Samples were imaged in a buffer containing 50
255 mM Cysteamine hydrochloride, 10% glucose, 0.6 mg/mL Glucose Oxidase from
256 Aspergillus niger, 0.063 mg/mL Catalase from Bovine liver in PBS, pH between 7.5-8.0.
257 Imaging was performed on a Zeiss Elyra P.1 TIRF microscope using a Zeiss alpha Plan

258 Apochromat TIRF 100x/1.46 NA oil objective and a tube lens providing an extra factor of
259 1.6x magnification. Alexa647 (or HyLite647) and CF568 dyes were imaged in
260 sequential time-series of approximately 20,000 frames each. Image size was 256x256
261 pixels, integration time was 18ms for both channels. Alexa-647 or HyLite547 molecules
262 were ground-state depleted and imaged with a 100mW 642 laser at 100% AOTF
263 transmission in ultra-high power mode (condensed field of illumination), corresponding
264 to approximately 1.4W/cm². Emission light passed through a LP655 filter. CF-568
265 molecules were ground-state depleted and imaged with a 200mW 561 laser at 100%
266 AOTF transmission in ultra-high power mode, corresponding to approximately
267 2.5W/cm². Emission light was passed through a BP 570-650 + LP 750 filter. For each
268 dye, ground-state return was elicited by continuous illumination with a 50mW 405 laser
269 at 0.01 to 0.1% AOTF transmission. Excitation light was filtered by a 405/488/561/642
270 filter placed in front of the camera. Images were recorded with an Andor iXon+ 897
271 EMCCD. The camera EM gain was set to 100, which yields an effective conversion of 1
272 photo electron into 1.65 digital units. The image pixel size was 100 nm xy.

273

274 *Processing:*

275 Raw data was processed through a custom pipeline written in MATLAB (Mathworks)
276 made up of a number of modular elements, described below. The Bio-Formats MATLAB
277 toolbox (Linkert et al., 2010) was used to read Zeiss raw data files into MATLAB. Image
278 data was transferred between MATLAB and FIJI using MIJI {ref:
279 <http://bigwww.epfl.ch/sage/soft/miji/>}. If necessary, raw data was pre-processed with a
280 temporal filter (Hoogendoorn et al.) to remove non-homogeneous background. The filter

281 radius was set at 51 frames, with a key frame distance of 10 (filter is explicitly calculated
282 only for every 10 frames and interpolated between), the quantile for the filtering was set
283 a 20%. Localization of dye emitters was performed using the ThunderSTORM ImageJ
284 plugin (Ovesny et al., 2014). The camera EM gain was set to 100, which resulted in a
285 photon-to-ADU of 1.65. When the temporal median filter was used, the Offset was set to
286 zero. Image filtering was done with the Wavelet filter setting, with a B-Spline order of 3
287 and scale of 2.0. A first pass approximate localization of molecules was achieved with
288 by finding local maximum with a peak intensity threshold of $2.5 * \text{std}(\text{Wave.F1})$ and 8-
289 neighborhood connectivity. Weighted least squares fitting of the PSF to achieve sub-
290 pixel localizations was achieved by use of an integrated Gaussian with a fitting radius of
291 4 pixels and an initial sigma of 1.5. Localizations were filtered based on the attributes of
292 uncertainty (<20 nm) and sigma (100 – 200 nm for CF568 and 90-190 for Alexa647 and
293 Hylite-647). Before each experiment a calibration was calculated to correct for shifts and
294 distortions between the acquired fluorescent channels. Sub-diffractive beads, labeled
295 with fluorophores in both channels were imaged. The bead positions were fitted and
296 registered between the fluorescent channels. Registered localizations from multiple
297 bead images were compiled into one data-set. Calibration matrices of the shift in x and
298 y direction between the imaging channels across the full field of view were calculated by
299 either applying a 2D polynomial fit or a localized weighted averaging to the registered
300 bead localizations. In the raw data, the shift and distortion between the imaging
301 channels was up to 100nm. Applying the calibration to the STORM data yields an RMS
302 error of less than 15nm for the channel misalignment. Drift correction was performed
303 using the redundant cross-correlation method described in (Wang et al., 2014). The

304 segmentation parameter was set at 500 frames, the bin size used in the cross-
305 correlation was 10nm, and the error threshold for the recalculation of the drift was 5
306 pixels.

307

308 *dSTORM analysis:*

309 Coordinate analysis of our dSTORM data is conceptually similar to methods previously
310 used to classify nanoscale organization at the excitatory synapse (Tang et al., 2016).

311 Synapses for downstream analysis were selected manually from a composite rendered
312 image and ROI coordinates were recorded using a custom ImageJ macro. ROI details

313 | were imported into MATLAB using the `ReadImageJROI` function

314 (ref:github.com/DylanMuir/ReadImageJROI). The post-synaptic density and synaptic A β
315 localization were segmented using a coordinate-by-coordinate density calculation.

316 Because labeling density could vary greatly, the thresholding parameter was
317 determined from the overall density range of the ROI. Localizations with a local-density
318 in the lower 10% of that range were considered to be outside of the synaptic

319 region/clusters. Boundaries for these regions were delineated using MATLAB's

320 `alphaShape` function, with an α value of 100. Only regions with an area of 1.5e3 nm² or
321 greater were considered for analysis. MATLAB's `inShape` function was used to

322 determine what percentage of A β or receptor localizations fell within the PSD boundary.
323 A β and receptor nanoclusters were defined by a cutoff determined by randomizing the

324 experimental localizations assuming a uniform distribution across the synaptic region.

325 The local density threshold for an experimental coordinate to be considered as part of a
326 nano-cluster was set at the mean local density of the randomized dataset plus 2

327 standard deviations. The geometric boundaries of individual nano-clusters were again
328 delineated using the `alphaShape` function, with an α value of 11. A β or receptor
329 nanoclusters were classified as overlapping with the PSD if the overlap area had a
330 fraction of 0.23 or greater of the total nanocluster area. The weighted center (mean of
331 coordinates) of each nanocluster was calculated and the center to PSD edge was
332 determined using the `nearestNeighbor` function. This distance was assigned as zero for
333 PSD overlapping nanoclusters.

334

335 *Code/Software*

336 All code used for super resolution image analysis is available at the links below:

337 STORM:

338 https://github.com/VvanL/structure_SMLM_analysisFile_fromSRPipeline_output

339 SIM:

340 <https://github.com/samanthalschwartz/NeuronAnalysisToolbox>

341

342 *Electrophysiology:*

343 Field recordings were performed as previously described using 2-3 week old C57BL/6
344 mice (Freund et al., 2016). Mice were sacrificed and brains rapidly removed and
345 immersed in ice-cold sucrose-containing cutting buffer (in mM: 2 KCl, 12 MgCl₂, 0.2
346 CaCl₂, 1.3 NaH₂PO₄, 10 D-glucose, 220 sucrose, 26 NaHCO₃, 1.77 sodium ascorbate, 2
347 N-acetylcysteine). Coronal slices containing hippocampus (400 μ m thickness) were
348 prepared using a McIlwain tissue chopper/slicer and recovered at 27°C for >60 min in
349 ACSF (in mM: 84.3 NaCl, 3 KCl, 1.8 CaCl₂, 1.3 NaH₂PO₄, 4.7 MgSO₄, 26 NaHCO₃, 10

350 glucose, 70.4 sucrose, 1.2 sodium ascorbate, 0.65 N-acetylcysteine). After recovery, a
351 single slice was transferred to a recording chamber and superfused with ACSF at a flow
352 rate of 2–3 ml/min at 31°C. The ACSF contained the following (in mM): 124 NaCl, 3.5
353 KCl, 1.3 MgCl₂, 2.5 CaCl₂, 1.3 NaH₂PO₄, 10 D-glucose, and 26 NaHCO₃. Field
354 recordings were made with a glass micropipette filled with ACSF placed in CA1 stratum
355 radiatum approximately 200–300 μm from the cell body layer. Synaptic fEPSPs were
356 evoked with bipolar tungsten electrodes placed in the Schaffer collateral axon pathway .
357 For each slice, an input–output curve was generated by increasing the stimulus voltage
358 and recording the synaptic response until either a maximum was reached or evidence of
359 a population spike was observed on the field excitatory postsynaptic potential (fEPSP)
360 response. The control stimulus intensity was set to 40% to 50% of the maximum
361 synaptic response, and a baseline recording was obtained delivering one test pulse
362 every 20 s for 20 min. To elicit LTP, we delivered two trains of 100 Hz stimuli lasting 1
363 second each, with an intertrain interval of 5 min. This protocol reliably produced LTP
364 that persisted for more than 45 min. We recorded the maximum amplitude of the
365 fEPSPs as well as their initial slopes, measured between 10% and 40% from the point
366 of negative deflection.

367

368 *Electron Microscopy and immunogold labeling*

369 For electron microscopy and immunogold labeling of neuronal cultures, we used
370 osmium-free processing as previously described (Phend et al 1995). Briefly, samples
371 were fixed with 2.5% glutaraldehyde in .1M Phosphate Buffer, and sequentially treated
372 with 1% tannic acid (EM sciences), 1% uranyl acetate, 1% PPD, .2% iridium

373 tetrabromide, and then were dehydrated and embedded for sectioning. Following
374 ultrathin microtome sectioning, samples were stained for antibodies against amyloid-
375 beta using previously described post-embed gold methods (Aoki, 2003). Briefly, grids,
376 were blocked in tris-buffered saline (.9% sodium chloride) containing 0.1% TritonX-100
377 (TBST, pH 7.6) and incubated in primary antibody diluted in TBST at room temperature
378 overnight. The following day, grids were washed with TBST and then blocked with
379 TBST, pH 8.2. Grids were incubated for 1 hour in donkey anti-mouse secondary
380 conjugated to 10 nm gold (EMS, 25825). Grids were washed, with TBST, H2O, post-
381 fixed with 1% glutaraldehyde, and counter-stained with Reynold's lead citrate.

382

383 *Expansion Microscopy (ExM)*

384 Samples were prepared according to the expansion microscopy protocol outlined in
385 (Zhang et al., 2020). Live DIV 16 hippocampal cultures were incubated with rabbit anti-
386 GluA1 for 10 min prior to fixation (Hiester et al., 2017; Kennedy et al., 2010) A β o (500
387 nM) was added to live cells for 15 min at 37°C. Cells were fixed for 15 min using 4%
388 paraformaldehyde (Electron Microscopy Sciences) and washed with PBS. Cells were
389 blocked for 30 min in PBS containing 5% bovine serum albumin (Sigma) and stained
390 with mouse anti-A β (6E10, Biolegend, 803014). Cells were then permeabilized with
391 0.2% TritonX-100 (Fisher Scientific) and incubated with guinea pig anti-bassoon
392 (Synaptic Systems, 141-004). Following incubation with secondary antibodies
393 (secondary antibodies were generated in goat and include anti-rabbit Alexa 488; anti-
394 rabbit Alexa 568; anti-guinea pig Alexa 488; anti-guinea pig Dylight 550; anti-mouse
395 Abberior Star 635) cells were exposed to a second round of fixation with 3% PFA/0.1%

396 glutaraldehyde (Electron Microscopy Sciences) and sequentially washed in 1X PBS and
397 distilled water. Acroloyl-X SE (AcX) (Invitrogen) diluted at 1:100 in PBS was added to
398 each well and cells were refrigerated overnight. On day 2 of the protocol, the AcX
399 solution was removed and coverslips were washed twice in 1X PBS for 5 min (samples
400 were placed on ice at the start of the second wash). Gelation solution was prepared by
401 combining chilled reagents: “Stock X” (Zhang et al., 2020), TEMED (Fisher
402 Bioreagents), and APS (Ammonium Persulfate) (Sigma) at a volumetric ratio of 98:1:1.
403 After removing PBS, 500 µL of gelation solution was added to each well for 5 min on
404 ice. Coverslips were then placed cell-side down atop a gelation chamber constructed
405 using a glass microscope slide and coverglass (Zhang et al., 2020). 60 µL of gelation
406 solution was quickly added underneath each coverslip, and the chambers incubated at
407 37° for 1 hour in a humidified chamber. Gelled samples were submerged in 10 mL
408 digestion buffer (Zhang et al., 2020) containing proteinase K in a 100 x 20 mm petri dish
409 (Corning) on an orbital shaker at 60 rpm at room temperature overnight. On day 3 of the
410 protocol, digestion buffer was removed and gels were incubated with 10 mL distilled
411 water on an orbital shaker at 60 RPM for 10 min to allow for gel expansion. This was
412 repeated 2 additional times. The expansion process was then repeated a third time, for
413 20 min. Following the final expansion step, gels were cut and plated on 35 x 10 mm
414 glass-bottom plates (Ted Pella) coated with 0.1% poly-L-lysine (Sigma). 2 mLs of
415 distilled water were then added to each plate and samples imaged on a spinning disc
416 confocal microscope.

417

418 *ExM Analysis*

419 A β distribution along the pre to postsynaptic axis was calculated using custom analysis
420 software in Matlab. Pre and postsynaptic proteins and A β puncta objects were
421 identified, labeled and the center of mass position was calculated as described in the
422 SIM analysis section of the methods. Synapses were filtered based on the following
423 criteria: 1) they contained both a pre and postsynaptic object, 2) there was an A β puncta
424 within 20 pixels in X-Y and 3 pixels in the Z dimension, and then further selected
425 manually based on the criterion that the synaptic alignment relative to the imaging plane
426 resulted in good separation between pre and post synaptic objects. Regions were
427 selected in ImageJ and imported into Matlab using the function 'ReadImageJROI.m'
428 ©Dylan Muir 2014. For each synapse, the center position for all A β puncta with 20
429 pixels in X-Y and 3 pixels in Z was mapped onto a cylindrical coordinate system having
430 a longitudinal axis defined by the vector between the post and presynaptic center of
431 mass positions with an origin at the midway point.

432

433 *Figure Processing:*

434 In some cases, images were expanded 2x and were interpolated for display only.
435 Volume-rendered images (Figs 2 and 4) were created using expanded, masked images
436 through the ImageJ volume viewer with a z-aspect of 2. All quantitative analysis was
437 performed on raw image files.

438

439 *Statistical analysis*

440 Statistical significance for experiments comparing two populations was determined
441 using a two-tailed unpaired Student's t-test. When populations were not normally

442 distributed, Mann-Whitney tests were used. In the cases where the two populations
443 represented paired measurements, a paired Student's t-test was used. For experiments
444 comparing three or more populations, a One-way ANOVA with Bonferroni multiple
445 comparison test was used. When populations were not normally distributed, Kruskal-
446 Wallis with Dunn's multiple comparisons test were used. Statistical analyses were
447 performed using GraphPad Prism and Microsoft excel. All data are presented as mean
448 \pm SEM unless otherwise stated.

449 **Results**

450 **A β o rapidly and stably accumulates on the cell surface at or near excitatory
451 synapses**

452 To directly visualize A β o as it binds to neurons, we generated fluorescently
453 labeled A β o using HiLyte647-labeled A β peptide as previously described (Lacor et al.,
454 2004; Sinnen et al., 2016). We confirmed the labeled peptide formed oligomeric species
455 by western blotting and that it blocked long-term potentiation (LTP) following high
456 frequency stimulation in acute mouse hippocampal slices (Extended Data Fig. 1-1).

457 We next characterized the rate of A β o binding and its stability at different
458 subcellular locations on excitatory neurons. Here we performed time lapse confocal
459 imaging as we applied labeled A β o (500 nM) to live dissociated hippocampal neurons
460 expressing mCherry (mCh) to visualize cellular morphology and a green fluorescent
461 protein (GFP)-labeled “fibronectin intrabody generated with mRNA display” (FingR)
462 against PSD95 (postsynaptic density protein 95; PSD95_{FingR}-GFP) to label excitatory
463 synapses (Fig. 1A). A β o binding was initially detected as diffraction-limited puncta within
464 seconds of A β o application. In most cases, A β puncta progressively grew in size and
465 intensity but saturated at a maximum plateau value within 5-10 min (Fig. 1B,C). Once
466 maximum binding was achieved, we observed detectable A β o signal overlapping with
467 64 \pm 6.8% of excitatory synapses, in agreement with previous studies (Lacor et al., 2004;
468 Sinnen et al., 2016). A β o binding was not exclusive to synapses; of the total A β o signal,
469 50 \pm 6.5% associated with dendritic spines and 50 \pm 6.5% associated with non-synaptic
470 sites on the dendritic shaft. Kinetic values for A β o accumulation at PSD95-positive
471 dendritic spines and non-synaptic sites were estimated by fitting binding curves with a

472 single exponential function (Fig. 1C); τ values for A β o association with dendritic spines
473 vs non-synaptic regions on dendritic shafts were similar; 3.62 ± 0.47 min and 3.51 ± 0.46
474 min respectively. However, when we compared maximum A β o fluorescence intensity at
475 PSD95-positive dendritic spines (10 min following A β o addition) with nearby non-
476 synaptic signal on the dendritic shaft, A β o signal was consistently elevated near PSD95,
477 suggesting a surface receptor(s) that is enriched at but not exclusive to excitatory
478 synapses (Fig 1C). A possible explanation for this enrichment is that A β o preferentially
479 associates with a structural feature unique to dendritic spines. Previous studies
480 proposed A β o binds directly to spine membranes by recognizing their degree of
481 curvature (Sugiura et al., 2015; Terakawa et al., 2018). Contrary to this hypothesis, we
482 found A β o accumulation at shaft excitatory synapses was not significantly different than
483 spine synapses (Fig. 1D,E). Thus, A β o appears to recognize a feature enriched at
484 excitatory synapses regardless of their localization or morphology.

485 We next measured the stability of A β o at synaptic and non-synaptic sites. Here
486 we added A β o to hippocampal neurons, allowed binding to saturate for ~10min, and
487 then washed the cells into A β o-free extracellular solution (Fig. 1F). Following washout,
488 A β o clusters remained highly stable at both synaptic and non-synaptic sites with only
489 $13.2 \pm 2.8\%$ (synaptic) or $12.7 \pm 3.3\%$ (non-synaptic) loss in signal after 15min (Fig 1G).
490 We also imaged samples that had been treated with A β o and then fixed to assess the
491 level of photobleaching over the same imaging time window and found photobleaching
492 could account for $2.2 \pm 1.1\%$ loss in signal. We also tested whether A β o remained on the
493 surface over the time course of this experiment by briefly applying an extracellular A β

494 antibody either 10 or 45 min following A β o application. In both cases we observed
495 nearly all (92.27 \pm 0.047% at 45 min) A β o puncta observed directly with HiLyte647-labeled
496 A β peptide co-labeled with the antibody signal. Thus, the observed stability was not the
497 result of internalization into stationary intracellular organelles (Fig. 1H,I).

498 In a complementary set of experiments, we performed fluorescence recovery
499 after photobleaching (FRAP) to investigate surface-bound A β o dynamics. Here we
500 applied A β o, waited 10 min to allow binding to saturate and then focally photobleached
501 individual A β o puncta at synaptic sites. When we performed FRAP measurements with
502 soluble A β o (500 nM) remaining in the ACSF, we observed limited but significant
503 recovery of bleached surface A β o clusters (synaptic A β o: mobile fraction=0.25 \pm 0.02,
504 recovery rate=0.15 \pm 0.03mins). Under these conditions, the source of signal recovery
505 could be soluble A β o from the extracellular solution, or laterally diffusing A β o that was
506 already associated with the cell surface (Renner et al., 2010). To distinguish these
507 possibilities, we performed additional FRAP measurements without A β o in the
508 extracellular solution to eliminate the soluble pool. Under these conditions, we observed
509 a ~4-fold decrease in the mobile fraction of bound A β o (0.059 \pm 0.015) at synaptic sites.
510 Thus, while surface-bound A β o appears stable at steady state, limited exchange with
511 soluble pools can occur (Fig 1J,K).

512

513 **Super resolution microscopy reveals A β o binds predominantly at perisynaptic
514 sites**

515 The nanoscale distribution of A β o surface binding remains poorly characterized.
516 We first used structured illumination microscopy (SIM) (Crosby et al., 2019; Gustafsson,

517 2005), which has approximately 2-fold higher resolution compared to confocal
518 microscopy as well as improved resolution in z, to localize A β o (500nM, applied 10min
519 prior to fixation) relative to the excitatory postsynaptic proteins GluA1 and PSD95,
520 detected by antibody staining (Fig. 2A). Surprisingly, our SIM images revealed that most
521 A β o surface clusters do not actually overlap with PSD95 or GluA1 signal as previously
522 reported in studies using wide field or confocal microscopy (Lacor et al., 2004; Renner
523 et al., 2010). Instead, most A β o signal appeared immediately adjacent to the PSD (Fig.
524 2B). In contrast, the synaptic receptor GluA1 appeared highly co-localized with PSD95,
525 confirming the observed perisynaptic localization of A β o was not due to optical or SIM
526 reconstruction artifacts (Fig. 2B). Using our SIM dataset, we also wanted to quantify the
527 degree to which total surface-bound A β o is enriched near excitatory synapses. We
528 developed an unbiased analysis routine that calculates the number of segmented A β o
529 clusters encountered at different voxel distances from a segmented synaptic marker
530 protein (Fig. 2C, see Methods for details). The number of A β o clusters at each distance
531 is then divided by a randomly simulated data set with the same labeling density. Thus, if
532 A β o binding is random with respect to the protein of interest, our analysis reports a
533 value of one. While there was little direct overlap between A β o and excitatory synaptic
534 proteins, we did observe a high degree of enrichment of total A β o signal within 200 nm
535 of excitatory synapses. As a control, we found no significant enrichment of A β o at
536 inhibitory synapses labeled with gephyrin, confirming specificity for excitatory synaptic
537 connections (Fig. 2D) (Lacor et al., 2004; Renner et al., 2010). Consistent with peri- or
538 extrasynaptic localization of bound A β o, our analyses yielded a much greater degree of
539 enrichment of the synaptic protein GluA1 near PSD95 (Fig. 2E).

540 To more precisely characterize the nanoscale organization of A β o binding with
541 respect to synapses, we used direct stochastic optical reconstruction microscopy
542 (dSTORM), which has 3-4-fold greater resolution than SIM (Heilemann et al., 2008).
543 Here we resolved A β o signal into discrete nanoscale clusters immediately adjacent to,
544 but generally non-overlapping with the postsynaptic density, labeled by immunostaining
545 PSD95 (Fig. 3A). On average, A β o-bound synapses were associated with 8.04 ± 1.36
546 A β o clusters, with individual clusters having an average area of $4548\pm600\text{nm}^2$. To
547 quantify the degree of A β o overlap with the PSD, we employed a density-based
548 clustering algorithm to define the PSD (based on a threshold density of PSD95
549 localizations) and then calculated the fraction of individual A β o localizations that fell
550 within the segmented PSD region (Fig. 3A). For comparison to a known synaptic
551 protein, we also performed this analysis with GluA1 (Fig. 3B). While $77\pm1.9\%$ of GluA1
552 localizations were observed within the PSD boundary, only $41\pm4.2\%$ of A β o
553 localizations fell within the PSD (Fig. 3C). We also performed a separate analysis where
554 we segmented discrete, spine-localized A β o clusters and quantified their percentage
555 overlap with the segmented PSD. Only 12.9% of spine A β o clusters fully overlapped
556 with the PSD compared to 50.9% for GluA1. Conversely, we observed that 61.1% of
557 spine A β o clusters were completely excluded from the PSD compared to only 28.7% for
558 GluA1 (Fig. 3D). Combined, our super resolution imaging data reveal the majority of
559 spine-localized A β o does not actually bind directly at the synaptic cleft, but localizes to
560 perisynaptic sites immediately adjacent to the PSD on the dendritic spine.
561

562

563 **A β o binds both pre- and post-synaptic membranes**

564 A β o is reported to rapidly disrupt both pre- and postsynaptic function, yet the
565 relative extent of direct A β o association with axonal terminals and dendritic spines
566 remains largely uncharacterized. To address this, we first performed post-embedding
567 immunogold electron microscopy (EM). We treated hippocampal cultures for 10-45 min
568 with A β o (500 nM) or an equal volume of PBS (negative control) prior to fixation.
569 Following fixation, embedding and cutting we labeled sections with an A β o antibody and
570 a gold-conjugated secondary antibody. We imaged samples by scanning EM and
571 quantified the number of gold particles per linear μ m of pre- or postsynaptic membrane
572 (Fig 4A). Given the estimated size of the primary and secondary antibodies (~10 nm
573 each), we only included gold particles that were within 20 nm of the plasma membrane.
574 Importantly, we observed little background signal in control (no added A β o) samples
575 (Fig. 4B). In samples treated with A β o, 32.5% and 67.5% of the total synaptic signal
576 was observed at the pre- and postsynaptic membrane respectively (Fig. 4C). Of the
577 total postsynaptic signal, ~75% was non-overlapping with the PSD, consistent with our
578 dSTORM and SIM data demonstrating perisynaptic binding (Figs. 3, 4D).

579 Given the sparse labeling and extensive fixation/processing steps required for
580 immunogold-EM, we took an independent fluorescence-based approach to quantify pre-
581 and postsynaptic A β o. We used expansion microscopy, which allows acquisition of
582 three or more fluorescent labels (an advantage over dSTORM) with higher spatial
583 resolution compared to SIM. We labeled live hippocampal neurons with A β o and then
584 fixed and stained for bassoon (presynaptic), GluA1 (postsynaptic) and A β and expanded

585 the preparation according to (Zhang et al., 2020) (Fig. 4E). Using cellular nuclei as a
586 reference, we estimate our samples were expanded 4-fold. We quantified A β o signal in
587 3 dimensions with respect to a plane perpendicular to an axis connecting the center of
588 mass of the segmented pre and postsynaptic signals (Fig. 4F, see Methods for details).
589 We found that 40.8% and 59.2% of A β o signal associated with the pre- and
590 postsynaptic label respectively, in agreement with our immunogold labeling. Once more,
591 A β o did not directly overlap with synaptic markers (Fig. E,F). Combined, these
592 experiments pinpoint A β o binding to sites immediately adjacent to the synaptic cleft with
593 significant amounts of A β o directly binding both pre- and postsynaptic compartments.

594

595 **Plasticity is disrupted specifically at A β o-bound spines**

596 While most synapses associate with A β o at the concentration used here (500
597 nM), a small fraction of spines do not appear to bind A β o. This allowed us to test
598 whether A β o selectively impairs synapses to which it is bound (Fig. 5A). One of the
599 hallmark synaptic pathologies of A β o is LTP impairment. LTP is associated with
600 structural enlargement of dendritic spines (sLTP) and can be locally triggered at
601 targeted synapses using focal 2-photon glutamate uncaging (Matsuzaki et al., 2004).
602 We used an established uncaging protocol (45 pulses, 0.5 Hz) to induce sLTP at
603 individual A β o-bound and A β o-free spines (Lee et al., 2009). In control cells that were
604 not treated with A β o, our glutamate uncaging protocol triggered robust and persistent
605 spine growth (Fig. 5B,C). A β o-bound spines from cells treated with A β o for 30-45 min
606 prior to sLTP induction initially exhibited a comparable degree of growth as controls, but
607 returned to baseline levels several minutes following plasticity induction. Surprisingly,

608 neighboring A β -free spines exhibited persistent growth that was indistinguishable from
609 control spines. In nearly every case, A β -free spines exhibited increased persistent
610 growth compared to nearby A β -bound spines on the same cell (Fig. 5D). Since the
611 extent of spine growth depends on initial size, we compared the average baseline sizes
612 (calculated as spine area from 2D projected images) of A β -bound and unbound spines
613 targeted for sLTP. There was no significant difference between the two populations
614 (A β -bound, $1.76 \pm .25 \mu\text{m}^2$; A β -free $1.69 \pm .19 \mu\text{m}^2$). Thus, A β disrupts plasticity in a
615 spatially restricted manner, presumably through local signaling mechanisms constrained
616 near sites of A β surface engagement.

617

618

619 **Discussion**

620 Increasing evidence supports a role for secreted, soluble A β o as the primary
621 culprit in AD-associated synapse dysfunction. While many studies have characterized
622 steady state A β distribution in human post-mortem samples and animal models, little is
623 known about the earliest steps of A β o-mediated synapse toxicity, including the spatial
624 and temporal dynamics of its engagement with the neuronal membrane. Here we used
625 a combination of live and high-resolution imaging modalities to define the rate, stability,
626 nanoscale localization and functional consequences of A β o binding.

627 To our knowledge, ours is the first to directly visualize A β o longitudinally as it
628 associates with neurons. This analysis revealed that A β o generally nucleates at specific
629 sites and attracts additional A β o with cluster growth saturating within minutes rather
630 than binding as discrete, pre-formed assemblies. Growth could occur through
631 recruitment of additional A β o from soluble pools and/or by coalescence of laterally
632 diffusing A β o/receptor complexes on the cell surface (Renner et al., 2010). In either
633 case, the rapid surface assembly and synaptic association we observe is consistent
634 with numerous observations that A β o can rapidly (within minutes) affect synaptic
635 function (Cook et al., 2019; Freund et al., 2016; Gulisano et al., 2019; Lauren et al.,
636 2009; Shankar et al., 2008; Um et al., 2012). It is important to note that we observed
637 little A β o internalization over this timescale, consistent with action through a signaling
638 surface receptor(s) rather than direct A β o-mediated interference of intracellular
639 plasticity-related processes. However, our data do not rule out an intracellular role for
640 A β o in pathologies that manifest over longer timescales, such as synapse elimination or

641 cell death (Takahashi et al., 2004; Takahashi et al., 2002). Indeed, numerous studies
642 have demonstrated accumulated intracellular pools of A β at synaptic sites in animal
643 models and human AD samples where A β is constitutively produced for months or
644 years (Koffie et al., 2009; Pickett et al., 2016).

645 While we focused on A β o binding at synaptic sites, it should be noted that A β o
646 accumulates at synaptic and non-synaptic sites with indistinguishable kinetics,
647 suggesting widespread and heterogeneous distribution of A β o receptor(s). The rate of
648 A β o binding was similar at spines and non-synaptic sites but surface A β o clusters were
649 consistently more intense near excitatory synapses suggesting some degree of receptor
650 enrichment at synaptic sites. While intriguing, the functional significance of synaptic A β o
651 binding has remained unclear. We demonstrate for the first time that A β o-bound spines
652 are more susceptible to plasticity disruption than neighboring A β o-free spines,
653 supporting a model where A β o engages locally restricted signaling mechanisms to
654 impair plasticity. Our experiments were performed over a relatively short timescale, with
655 application of A β o approximately 30 min prior to plasticity induction. It remains possible
656 that longer, disease relevant exposure times would lead to more global plasticity
657 disruption. It will also be important to investigate whether other aspects of A β o-mediated
658 pathology, such as synapse loss, occur selectively at sites where A β o initially engages
659 the neuronal surface. In any case, these results emphasize the importance of future
660 experiments unraveling molecular features that shield select synapses from A β o binding
661 and subsequent plasticity deficits.

662 Our experiments are also the first to map the nanoscale distribution of A β o
663 surface engagement. The imaging techniques used in earlier studies lacked the spatial

664 resolution to precisely map A β o binding sites (Koffie et al., 2009; Lacor et al., 2004;
665 Renner et al., 2010; Um et al., 2012). Surprisingly, we observed very little A β o actually
666 binds directly at the postsynaptic density. Instead, A β o forms nanoscale clusters
667 immediately adjacent to and surrounding the excitatory synaptic cleft. Several reported
668 A β o receptors localize to perisynaptic regions, including α 7 nicotinic acetylcholine
669 receptor (α 7-nAChR), cellular prion protein (PrP^c) and metabotropic glutamate receptor
670 5 (mGluR5) (Jones & Wonnacott, 2004; Luján et al., 1996; Mironov et al., 2003).
671 Perisynaptic localization also suggests A β o is unlikely to exert its effects through direct
672 binding of synaptic neurotransmitter receptors such as NMDA or AMPA-type glutamate
673 receptors as previously proposed (De Felice et al., 2007; Lacor et al., 2007; Texido et
674 al., 2011; Zhao et al., 2010). While earlier studies concluded A β o binds primarily to
675 postsynaptic sites on dendritic spines, these experiments primarily relied on diffraction
676 limited imaging techniques. Using multiple approaches, we confirmed binding near the
677 postsynaptic membrane but also observed a substantial fraction of A β o binding to
678 axonal terminals, consistent with rapid A β o-mediated effects on presynaptic vesicle
679 release probability, glutamate reuptake and structural alterations (Abramov et al., 2009;
680 He et al., 2019; Huang et al., 2013). Whether the same receptor mediates A β o binding
681 to both pre- and postsynaptic compartments is unknown, but several reported A β o
682 receptors localize to both sides of the synapse, including α 7-nAChR and PrP^c (Barmada
683 et al., 2004; Fabian-Fine et al., 2001; Moya et al., 2000; Um et al., 2013; Um et al.,
684 2012).

685 Taken together, our study is the first to interrogate the kinetics, stability,
686 ultrastructural localization and functional consequences of A β o binding. These basic,

687 yet fundamental assessments provide new insight into the earliest steps of A β o toxicity
688 and lay the groundwork for future studies evaluating the relevant receptor(s) responsible
689 for neuronal surface engagement and the local signaling mechanisms leading to
690 synapse dysfunction.

691

692 **Acknowledgements:** The authors wish to thank Chandra Tucker for critical discussions
693 in preparing this manuscript. We would also like to acknowledge the University of
694 Colorado Advanced Light Microscopy Core Facility. The work was supported by
695 National Institute of Neurological Disorders and Stroke R35NS116879 (M.J.K.);
696 NS110383 (M.J.K., M.L.D.); National Institute on Aging T32AG000279 (H.S.A.);
697 AG058005 (M.J.K.) and National Institute of Mental Health R01MH119154 (K.R.S.).
698

699

700 **Figure 1: Kinetics of A β association and dissociation at synaptic sites**

701 **A.** Representative dendritic segment from a neuron transfected with mCherry (red) and

702 PSD95_{FingR}-GFP (green) treated with labeled A β o (teal) for 10 min. Closed arrowheads

703 denote dendritic spines labeled with A β o and the open arrowhead denotes a spine

704 lacking A β o. Fluorescent A β was confirmed to form oligomeric species and block LTP in

705 Extended Data Figure 1-1. Scale bar = 1 μ m

706 **B.** Representative image series of A β o accumulation on a spine excitatory synapse.

707 A β o was added at 0 s. Scale bar = 1 μ m

708 **C.** (Left) Quantification of A β o association kinetics at PSD95-positive dendritic spines or

709 neighboring PSD95-negative dendritic shafts (n=10 neurons, 4 independent cultures).

710 (Right) Peak average F/F₀ values for A β o binding at PSD95+ vs. PSD95- (shaft)

711 locations on the same cell (n= 10 neurons; p=0.0139, paired Student's t-test).

712 **D.** Representative image of A β o localization to spine (arrow) and shaft (arrowhead)

713 PSD95. Scale bar = 1 μ m.

714 **E.** (Left) A β o binding kinetics at PSD95 puncta on spines or shafts (n=20 PSD95 puncta

715 from 5 neurons, 3 independent cultures). (Right) Plateau intensity values of A β o at

716 PSD95 puncta on the spine and shaft of the same neuron (n=5 neurons, p=0.2857,

717 paired Student's t-test).

718 **F.** Representative image sequence of A β o (teal) bound to a dendritic spine following

719 washout into A β o-free imaging media at t=0 min. The cell outline is shown as a dashed

720 line, drawn based on a cell fill (not shown). Scale bar = 1 μ m

721 **G.** Quantification of A β o intensity following washout. Data are plotted as F/F₀, with F₀
722 representing normalized A β o signal immediately prior to washout (n=5 neurons).

723 **H.** Representative image of a dendrite from a hippocampal neuron expressing mCh
724 (dotted line), treated with labeled A β o (cyan, left panel) for 10 min and then an
725 extracellular antibody against A β o to assess surface localization (green). Scale bar =
726 1 μ m

727 **I.** Fraction of A β o puncta (averaged per cell) labeled with an extracellular antibody (i.e.
728 localized to the cell surface) 10 and 45 min following A β o application (n=5 neurons per
729 group, two independent cultures). ns=not significant, Student's t-test.

730 **J.** Representative time series for FRAP experiments. Shown is a single A β o-bound
731 spine. The A β o signal was photobleached and signal recovery was monitored over time.
732 Arrowheads indicate the location of photobleaching and signal recovery. Scale bar = 1
733 μ m.

734 **K.** Kinetics and extent of A β o recovery following photobleaching in the continued
735 presence (no wash, orange) or absence (wash, red) of A β o in the extracellular solution
736 (wash: n= 23 spines, from 6 neurons and 2 independent cultures; no wash: n=12 spines
737 from 4 neurons and 2 independent cultures). Quantification of the mobile A β o fraction is
738 shown to the right under each condition (**p=0.0007, Student's t-test).

739

740 **Figure 2. Super resolution localization of A β o relative to excitatory and inhibitory**
741 **synapses.**

742 **A.** Representative SIM images of A β o (teal) with excitatory synaptic proteins PSD95
743 (yellow), GluA1 (red) and the inhibitory synaptic protein Gephyrin (green). Bottom
744 panels show control, GluA1 (red) with PSD95 (yellow). Scale bars = 1um.

745 **B.** Expanded regions showing individual synapses from panel A. Scale bars = 500 nm.
746 The graphs to the right of each example plot pixel intensities for each channel along a
747 line drawn diagonally through representative synapses. 3-dimensional volume
748 renderings of masked and segmented synapses are shown to the right.

749 **C.** Approach for quantifying the spatial relationship between synaptic proteins and A β o.
750 i. Representative SIM image showing PSD95 (green) and A β o (cyan). The outline of the
751 cell (dashed line) was drawn using the signal from an mCh cell fill (not shown). ii. The
752 A β o signal (cyan) is masked and binarized (blue); Right, PSD95 (green) is masked and
753 binarized. iii. Magnified red box from ii. The number of A β o puncta are counted at
754 increasing concentric voxel distances around masked synaptic marker.

755 **D.** The number of A β o puncta (quantified as described in panel B) at different distances
756 from either PSD95 (orange; n=48 neurons) or gephyrin (green; n=18 neurons),
757 normalized to randomly localized simulated data (black; average of 7 independent
758 simulations). A value of 1 indicates no spatial relationship, >1 a positively correlated
759 spatial relationship, and <1 a negatively correlated spatial relationship.

760 **E.** A β o is enriched near the excitatory PSD. Plotted is the average number density of
761 segmented A β o puncta 0-64nm from PSD95, GluA1 or gephyrin (PSD95 n= 48
762 neurons, GluA1 n=16 neurons, gephyrin n=18 neurons). The average number density of
763 the synaptic protein GluA1 relative to PSD95 is plotted for comparison (n=7 neurons).
764 ***p<0.0001, one-way ANOVA.

765

766 **Figure 3: Single molecule localization microscopy reveals A β o forms nanoscale
767 clusters immediately adjacent to the synaptic membrane**

768 A. Representative dSTORM images of synapses from hippocampal neurons labeled
769 with PSD95 (magenta) that were treated with 500 nM A β o (cyan) for 10 min. Three
770 examples of raw localization data are shown. The bottom panels display localizations
771 using a density-based lookup table with warmer colors representing higher density
772 regions. The segmented PSD is shaded in grey. Scale bar = 200 nm.

773 B. Representative dSTORM image of GluA1 (cyan) and PSD95 (magenta). Raw
774 localizations are shown in the top panels and the bottom panels are rendered as in (A).
775 Scale bar = 200 nm.

776 C. Quantification of the fraction of individual spine A β o localizations that fall within the
777 segmented PSD95 at single synapses (left; n=24 synapses, 5 cells, 2 independent
778 cultures). The same analysis is shown for GluA1 for comparison (right; n=64 synapses,
779 11 cells, 3 independent cultures). ***p<0.0001, Students t-test.

780 D. Frequency histograms are shown plotting the fraction overlap of segmented A β o
781 clusters (left) or GluA1 clusters (right) with the PSD. A value of 0 indicates no overlap
782 with the PSD while a value of 1 indicates the cluster fell entirely within the PSD.
783 Intermediate values indicate clusters that fell on the edge of the segmented PSD.

784

785 **Figure 4: A β o binds at both pre- and postsynaptic sites**

786 A. Representative post-embedding immunogold electron micrograph of a synapse
787 exposed to 500nM A β o and labeled with an A β antibody and gold-conjugated

788 secondary. The green box (magnified in inset) highlights immunogold signal. Gold
789 particles within 20 nm of the cell membrane were considered plasma membrane-
790 associated based on the size of the primary and secondary labeling antibodies. Scale
791 bar, 200nm.

792 B. Quantification of total membrane-associated A β o (measured as total number of gold
793 particles per linear micron of plasma membrane) from samples treated with PBS alone
794 or PBS with 500 nM A β o. (PBS: n=60 spines; A β : n=66 spines; p<0.0001, Mann-
795 Whitney test).

796 C. Quantification of A β o label on the pre- or postsynaptic membrane (p=0.0005, Mann-
797 Whitney test).

798 D. Percentage of the total dendritic spine gold particles that localized directly at the PSD
799 or perisynaptic regions within 200nm of the PSD (n=27 gold particles).

800 E. Representative image of a dendritic segment processed for expansion microscopy
801 (ExM), labeled for presynaptic bassoon (green), postsynaptic GluA1 (red), and A β o
802 (cyan). The lower panels show two representative synapses (labeled 1 and 2) from the
803 larger image and their respective 3-dimensional volume renderings.

804 F. (Top) Schematic of the analysis used to quantify pre- and postsynaptic A β o signal.
805 The synaptic axis is defined by a line drawn between the centers of mass of masked
806 bassoon (presynaptic marker) and GluA1 (postsynaptic marker) signals. A vector is
807 generated from the middle of the pre/post axis to the center of mass of the segmented
808 A β o, with the component vectors representing the radial distance from the synapse
809 center (r) and the distance along the pre/post axis (z). (Bottom) Quantification of A β o
810 signal along the pre/post and radial axes. Negative and positive values indicate post-

811 and presynaptic localization respectively. The number of A β o puncta at different
812 distances along the pre/post axis are summed and plotted in the histogram to the right
813 (n= 89 synapses from 26 neurons from 3 independent cultures).

814

815 **Figure 5: A β o-mediated plasticity impairment is locally restricted near sites of**
816 **surface binding**

817 A. (Left) Representative image of a dendritic segment from a neuron transfected with
818 tdTomato (red) and treated with A β o-488 (teal). Asterisks designate the location of MNI-
819 glutamate uncaging. The closed arrowhead shows a spine with bound A β o (A β +) , and
820 the open arrowhead shows a neighboring spine lacking A β o (A β -). (Right) Time course
821 of A β o- spine (top) and A β o+ spine (bottom) from the same dendritic segment before
822 the uncaging stimulus and up to 24 min following the stimulus. Scale bars = 5 μ m, left
823 panel; 1 μ m, right panels.

824 B. Quantification of spine size (based on the cell fill intensity) before and after MNI-
825 glutamate uncaging for control spines not treated with A β o (blue, n= 14 spines, N= 5
826 neurons, 3 independent cultures), adjacent spines that were not stimulated (green, n=
827 12 spines, N= 5 neurons, 3 independent cultures), A β + spines from cultures treated with
828 500nM A β o for at least 25 min (maroon, n=16 spines, N=8 neurons, 3 independent
829 cultures), and neighboring A β o-lacking spines (black, n=14 spines, 8 neurons, 3
830 independent cultures).

831 C. Average increase in spine cell fill signal during the final 3 min of imaging compared to
832 baseline for control (n=14 spines, N= 5 neurons, 3 independent cultures), A β o+ (n=16

833 spines, N=8 neurons, 3 independent cultures) and A β o- (n=14 spines, 8 neurons, 3
834 independent cultures) (*p≤ 0.05, Student's t-test).

835 D. Average F/F₀ over the final 3 min of imaging compared to baseline at A β o-bound
836 spines and neighboring A β o-free spines on the same neurons (8 neurons, 3
837 independent cultures, *p=0.0116, Paired t-test).

838

839

840 **Extended Data Figure Legend:**

841 **Figure 1-1. Fluorescent A β peptide forms oligomers that disrupt LTP.**

842 A. HiLyte647-conjugated A β peptide forms oligomeric species. Shown is an immunoblot
843 (probed with anti-A β 6E10) of A β o prepared with HiLyte647-labeled peptide. Note the
844 presence of putative dimers (1), trimers (2) and higher molecular weight species (3) in
845 the preparation.

846 B. A β o prepared with HiLyte647-labeled peptide disrupts LTP measured by EPSP slope
847 (left) or peak EPSP amplitude (right). LTP was induced by delivering 2 x 1 s trains of
848 100Hz stimulation spaced 5 min apart (arrows). Slices were exposed to A β o for 20 min
849 prior to LTP induction. n= 8 slices from 8 animals, control; 6 slices from 6 animals A β o-
850 treated.

851 C. Representative EPSPs from control (left) or A β o-treated (right) slices before (black)
852 and 45 min following (gray) LTP induction.

853 D. Average EPSP slope (left) and amplitude (right) for control (PBS treated) or A β o-
854 treated slices 45 min following LTP induction. The dashed line represents baseline.
855 *p<0.05, Student's t-test.

856

857 **Bibliography**

- 858 Abramov, E., Dolev, I., Fogel, H., Ciccotosto, G. D., Ruff, E., & Slutsky, I. (2009).
859 Amyloid-beta as a positive endogenous regulator of release probability at
860 hippocampal synapses. *Nat Neurosci*, 12(12), 1567-1576.
861 <https://doi.org/10.1038/nn.2433>
- 862
- 863 Aoki, C., Fujisawa, S., Mahadomrongkul, V., Shah, P., Nader, K., Erisir, A. (2003).
864 NMDA receptor blockade in intact adult cortex increases trafficking of NR2A
865 subunits into spines, postsynaptic densities, and axon terminals. *Brain*
866 *Research*(963), 139-149.
- 867
- 868 Barmada, S., Piccardo, P., Yamaguchi, K., Ghetti, B., & Harris, D. A. (2004). GFP-
869 tagged prion protein is correctly localized and functionally active in the brains of
870 transgenic mice. *Neurobiol Dis*, 16(3), 527-537.
871 <https://doi.org/10.1016/j.nbd.2004.05.005>
- 872
- 873 Cook, S. G., Goodell, D. J., Restrepo, S., Arnold, D. B., & Bayer, K. U. (2019).
874 Simultaneous Live Imaging of Multiple Endogenous Proteins Reveals a
875 Mechanism for Alzheimer's-Related Plasticity Impairment. *Cell Rep*, 27(3), 658-
876 665 e654. <https://doi.org/10.1016/j.celrep.2019.03.041>
- 877
- 878 Crosby, K. C., Gookin, S. E., Garcia, J. D., Hahm, K. M., Dell'Acqua, M. L., & Smith, K.
879 R. (2019). Nanoscale Subsynaptic Domains Underlie the Organization of the
880 Inhibitory Synapse. *Cell Rep*, 26(12), 3284-3297 e3283.
881 <https://doi.org/10.1016/j.celrep.2019.02.070>
- 882
- 883 De Felice, F. G., Velasco, P. T., Lambert, M. P., Viola, K., Fernandez, S. J., Ferreira, S.
884 T., & Klein, W. L. (2007). Abeta oligomers induce neuronal oxidative stress
885 through an N-methyl-D-aspartate receptor-dependent mechanism that is blocked
886 by the Alzheimer drug memantine. *J Biol Chem*, 282(15), 11590-11601.
887 <https://doi.org/10.1074/jbc.M607483200>
- 888
- 889 Dekosky, S. a. S., SW. (1990). Synapse Loss in Frontal Cortex Biopsies in Alzheimer's
890 Disease: Correlation with Cognitive Severity. *Ann Neurol*, 27, 457-464.
- 891
- 892 Fabian-Fine, R., Skehel, P., Errington, M. L., Davies, H. A., Sher, E., Stewart, M. G., &
893 Fine, A. (2001). Ultrastructural distribution of the alpha7 nicotinic acetylcholine
894 receptor subunit in rat hippocampus. *J Neurosci*, 21(20), 7993-8003.
895 <https://doi.org/10.1523/JNEUROSCI.21-20-07993.2001>
- 896
- 897 Freund, R. K., Gibson, E. S., Potter, H., & Dell'Acqua, M. L. (2016). Inhibition of the
898 Motor Protein Eg5/Kinesin-5 in Amyloid beta-Mediated Impairment of
899 Hippocampal Long-Term Potentiation and Dendritic Spine Loss. *Mol Pharmacol*,
900 89(5), 552-559. <https://doi.org/10.1124/mol.115.103085>

- 901
902 Games, D., Adams, D., Alessandrini, R., Barbour, R., Berthelette, P., Blackwell, C.,
903 Carr, T., Clemens, J., Donaldson, T., Gillespie, F., & et al. (1995). Alzheimer-type
904 neuropathology in transgenic mice overexpressing V717F beta-amyloid
905 precursor protein. *Nature*, 373(6514), 523-527. <https://doi.org/10.1038/373523a0>
- 906
907 Gong, Y., Chang, L., Viola, K. L., Lacor, P. N., Lambert, M. P., Finch, C. E., Krafft, G.
908 A., & Klein, W. L. (2003). Alzheimer's disease-affected brain: presence of
909 oligomeric A beta ligands (ADDLs) suggests a molecular basis for reversible
910 memory loss. *Proc Natl Acad Sci U S A*, 100(18), 10417-10422.
911 <https://doi.org/10.1073/pnas.1834302100>
- 912
913 Gulisano, W., Melone, M., Ripoli, C., Tropea, M. R., Li Puma, D. D., Giunta, S., Cocco,
914 S., Marcotulli, D., Origlia, N., Palmeri, A., Arancio, O., Conti, F., Grassi, C., &
915 Puzzo, D. (2019). Neuromodulatory Action of Picomolar Extracellular Abeta42
916 Oligomers on Presynaptic and Postsynaptic Mechanisms Underlying Synaptic
917 Function and Memory. *J Neurosci*, 39(30), 5986-6000.
918 <https://doi.org/10.1523/JNEUROSCI.0163-19.2019>
- 919
920 Gustafsson, M. G. (2005). Nonlinear structured-illumination microscopy: wide-field
921 fluorescence imaging with theoretically unlimited resolution. *Proc Natl Acad Sci U
922 S A*, 102(37), 13081-13086. <https://doi.org/10.1073/pnas.0406877102>
- 923
924 He, Y., Wei, M., Wu, Y., Qin, H., Li, W., Ma, X., Cheng, J., Ren, J., Shen, Y., Chen, Z.,
925 Sun, B., Huang, F. D., Shen, Y., & Zhou, Y. D. (2019). Amyloid beta oligomers
926 suppress excitatory transmitter release via presynaptic depletion of
927 phosphatidylinositol-4,5-bisphosphate. *Nat Commun*, 10(1), 1193.
928 <https://doi.org/10.1038/s41467-019-09114-z>
- 929
930 Heilemann, M., van de Linde, S., Schuttpelz, M., Kasper, R., Seefeldt, B., Mukherjee,
931 A., Tinnefeld, P., & Sauer, M. (2008). Subdiffraction-resolution fluorescence
932 imaging with conventional fluorescent probes. *Angew Chem Int Ed Engl*, 47(33),
933 6172-6176. <https://doi.org/10.1002/anie.200802376>
- 934
935 Hiester, B. G., Bourke, A. M., Sinnen, B. L., Cook, S. G., Gibson, E. S., Smith, K. R., &
936 Kennedy, M. J. (2017). L-Type Voltage-Gated Ca(2+) Channels Regulate
937 Synaptic-Activity-Triggered Recycling Endosome Fusion in Neuronal Dendrites.
938 *Cell Rep*, 21(8), 2134-2146. <https://doi.org/10.1016/j.celrep.2017.10.105>
- 939
940 Hoogendoorn, E., Crosby, K. C., Leyton-Puig, D., Breedijk, R. M., Jalink, K., Gadella, T.
941 W., & Postma, M. (2014). The fidelity of stochastic single-molecule super-
942 resolution reconstructions critically depends upon robust background estimation.
943 *Sci Rep*, 4, 3854. <https://doi.org/10.1038/srep03854>
- 944
945 Huang, J. K., Ma, P. L., Ji, S. Y., Zhao, X. L., Tan, J. X., Sun, X. J., & Huang, F. D.
946 (2013). Age-dependent alterations in the presynaptic active zone in a Drosophila

- 947 model of Alzheimer's disease. *Neurobiol Dis*, 51, 161-167.
948 <https://doi.org/10.1016/j.nbd.2012.11.006>
- 949
- 950 Jones, I. W., & Wonnacott, S. (2004). Precise localization of alpha7 nicotinic
951 acetylcholine receptors on glutamatergic axon terminals in the rat ventral
952 tegmental area. *J Neurosci*, 24(50), 11244-11252.
953 <https://doi.org/10.1523/JNEUROSCI.3009-04.2004>
- 954
- 955 Kennedy, M. J., Davison, I. G., Robinson, C. G., & Ehlers, M. D. (2010). Syntaxin-4
956 defines a domain for activity-dependent exocytosis in dendritic spines. *Cell*,
957 141(3), 524-535. <https://doi.org/10.1016/j.cell.2010.02.042>
- 958
- 959 Klein, W. L. (2002). A β toxicity in Alzheimer's disease: globular oligomers(ADDLs) as
960 new vaccine and drug targets. *Neurochem Int*, 41, 345-352.
- 961
- 962 Koffie, R. M., Meyer-Luehmann, M., Hashimoto, T., Adams, K. W., Mielke, M. L.,
963 Garcia-Alloza, M., Micheva, K. D., Smith, S. J., Kim, M. L., Lee, V. M., Hyman, B.
964 T., & Spires-Jones, T. L. (2009). Oligomeric amyloid beta associates with
965 postsynaptic densities and correlates with excitatory synapse loss near senile
966 plaques. *Proc Natl Acad Sci U S A*, 106(10), 4012-4017.
967 <https://doi.org/10.1073/pnas.0811698106>
- 968
- 969 Lacor, P. N., Buniel, M. C., Chang, L., Fernandez, S. J., Gong, Y., Viola, K. L., Lambert,
970 M. P., Velasco, P. T., Bigio, E. H., Finch, C. E., Krafft, G. A., & Klein, W. L.
971 (2004). Synaptic targeting by Alzheimer's-related amyloid beta oligomers. *J
972 Neurosci*, 24(45), 10191-10200. <https://doi.org/10.1523/JNEUROSCI.3432-04.2004>
- 973
- 974
- 975 Lacor, P. N., Buniel, M. C., Furlow, P. W., Clemente, A. S., Velasco, P. T., Wood, M.,
976 Viola, K. L., & Klein, W. L. (2007). Abeta oligomer-induced aberrations in
977 synapse composition, shape, and density provide a molecular basis for loss of
978 connectivity in Alzheimer's disease. *J Neurosci*, 27(4), 796-807.
979 <https://doi.org/10.1523/JNEUROSCI.3501-06.2007>
- 980
- 981 Lambert, M. P., Barlow, A. K., Chromy, B. A., Edwards, C., Freed, R., Liosatos, M.,
982 Morgan, T. E., Rozovsky, I., Trommer, B., Viola, K. L., Wals, P., Zhang, C.,
983 Finch, C. E., Krafft, G. A., & Klein, W. L. (1998). Diffusible, nonfibrillar ligands
984 derived from Abeta1-42 are potent central nervous system neurotoxins. *Proc Natl
985 Acad Sci U S A*, 95(11), 6448-6453. <https://doi.org/10.1073/pnas.95.11.6448>
- 986
- 987 Lauren, J., Gimbel, D. A., Nygaard, H. B., Gilbert, J. W., & Strittmatter, S. M. (2009).
988 Cellular prion protein mediates impairment of synaptic plasticity by amyloid-beta
989 oligomers. *Nature*, 457(7233), 1128-1132. <https://doi.org/10.1038/nature07761>
- 990

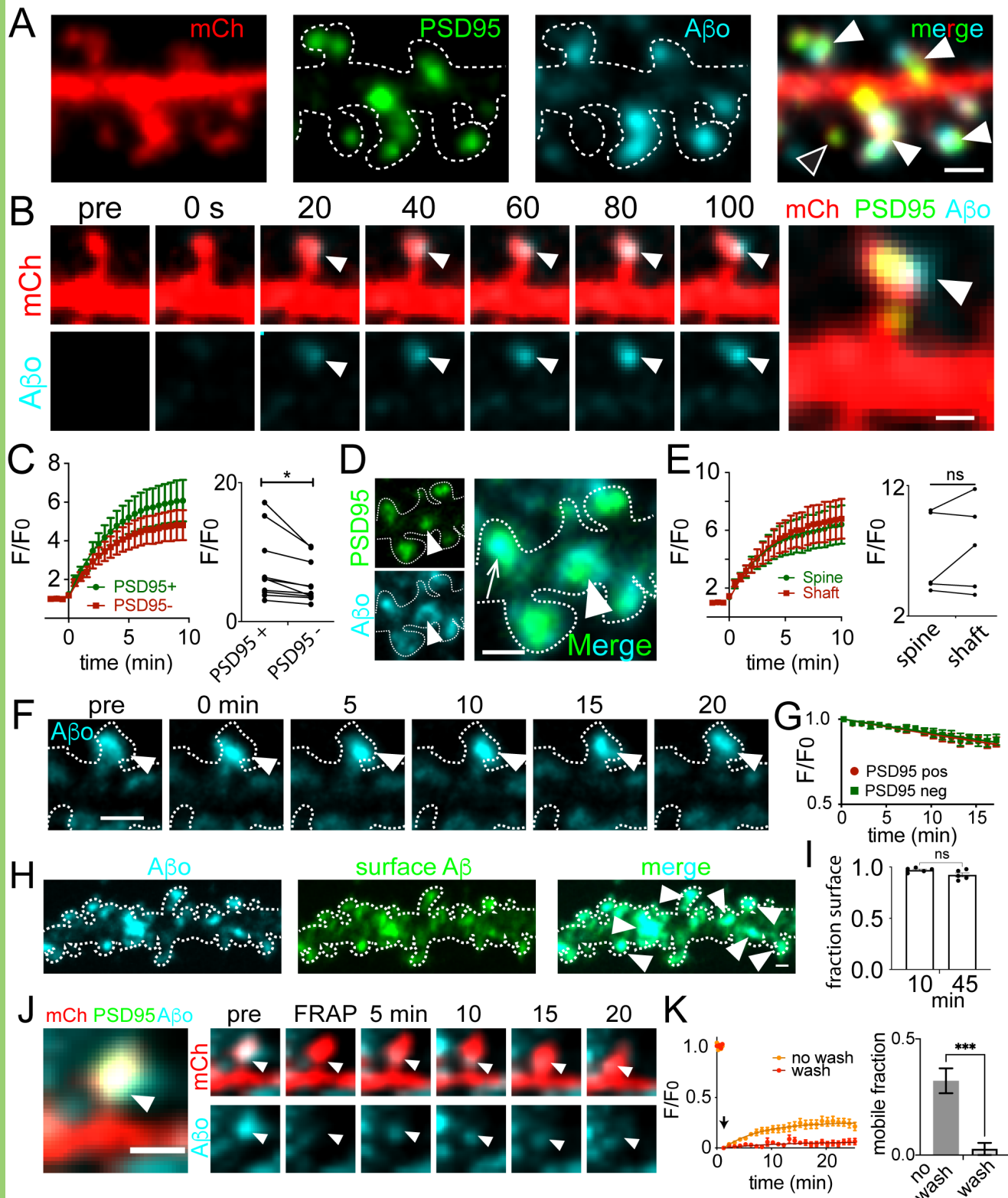
- 991 Lee, S. J., Escobedo-Lozoya, Y., Szatmari, E. M., & Yasuda, R. (2009). Activation of
992 CaMKII in single dendritic spines during long-term potentiation. *Nature*,
993 458(7236), 299-304. <https://doi.org/10.1038/nature07842>
- 994
- 995 Lesne, S., Koh, M. T., Kotilinek, L., Kayed, R., Glabe, C. G., Yang, A., Gallagher, M., &
996 Ashe, K. H. (2006). A specific amyloid-beta protein assembly in the brain impairs
997 memory. *Nature*, 440(7082), 352-357. <https://doi.org/10.1038/nature04533>
- 998
- 999 Linkert, M., Rueden, C. T., Allan, C., Burel, J. M., Moore, W., Patterson, A., Loranger,
1000 B., Moore, J., Neves, C., Macdonald, D., Tarkowska, A., Sticco, C., Hill, E.,
1001 Rossner, M., Elceiri, K. W., & Swedlow, J. R. (2010). Metadata matters: access
1002 to image data in the real world. *J Cell Biol*, 189(5), 777-782.
1003 <https://doi.org/10.1083/jcb.201004104>
- 1004
- 1005 Luján, R., Nusser, Z., Roberts, J. D. B., Shigemoto, R., & Somogyi, P. (1996).
1006 Perisynaptic Location of Metabotropic Glutamate Receptors mGluR1 and
1007 mGluR5 on Dendrites and Dendritic Spines in the Rat Hippocampus. *European
1008 Journal of Neuroscience*, 8(7), 1488-1500.
1009 <https://doi.org/https://doi.org/10.1111/i.1460-9568.1996.tb01611.x>
- 1010
- 1011 Matsuzaki, M., Honkura, N., Ellis-Davies, G. C., & Kasai, H. (2004). Structural basis of
1012 long-term potentiation in single dendritic spines. *Nature*, 429(6993), 761-766.
1013 <https://doi.org/10.1038/nature02617>
- 1014
- 1015 Mironov, A., Latawiec, D., Wille, H., Bouzamondo-Bernstein, B., Legname, G.,
1016 Williamson, R., Burton, D., DeArmond, S., Prusiner, S., & Peters, P. (2003).
1017 Cytosolic Prion Protein in Neurons. *The Journal of Neuroscience*, 23(18), 7183-
1018 7193. <https://doi.org/10.1523/JNEUROSCI.23-18-07183.2003>
- 1019
- 1020 Moya, K., Sales, N., Hassig, R., Creminon, C., Grassi, J., & Di Giambardino, L.
1021 (2000). Immunolocalization of the Cellular Prion Protein in Normal Brain.
1022 *Microscopy Research and Technique*, 50, 58-65.
- 1023
- 1024 Ovesny, M., Krizek, P., Borkovec, J., Svindrych, Z., & Hagen, G. M. (2014).
1025 ThunderSTORM: a comprehensive ImageJ plug-in for PALM and STORM data
1026 analysis and super-resolution imaging. *Bioinformatics*, 30(16), 2389-2390.
1027 <https://doi.org/10.1093/bioinformatics/btu202>
- 1028
- 1029 Pickett, E. K., Koffie, R. M., Wegmann, S., Henstridge, C. M., Herrmann, A. G., Colom-
1030 Cadena, M., Lleo, A., Kay, K. R., Vaught, M., Soberman, R., Walsh, D. M.,
1031 Hyman, B. T., & Spires-Jones, T. L. (2016). Non-Fibrillar Oligomeric Amyloid- β
1032 within Synapses. *Journal of Alzheimer's Disease*, 53, 787-800.
1033 <https://doi.org/10.3233/JAD-160007>
- 1034
- 1035 Renner, M., Lacor, P. N., Velasco, P. T., Xu, J., Contractor, A., Klein, W. L., & Triller, A.
1036 (2010). deleterious effects of amyloid beta oligomers acting as an extracellular

- 1037 scaffold for mGluR5. *Neuron*, 66(5), 739-754.
1038 <https://doi.org/10.1016/j.neuron.2010.04.029>
- 1039
- 1040 Seubert, P., Vigo-Pelfrey, C., Esch, F., Lee, M., Dovey, H., Davis, D., Sinha, S.,
1041 Schlossmacher, M., Whaley, J., Swindlehurst, C., & et al. (1992). Isolation and
1042 quantification of soluble Alzheimer's beta-peptide from biological fluids. *Nature*,
1043 359(6393), 325-327. <https://doi.org/10.1038/359325a0>
- 1044
- 1045 Shankar, G. M., Bloodgood, B. L., Townsend, M., Walsh, D. M., Selkoe, D. J., &
1046 Sabatini, B. L. (2007). Natural oligomers of the Alzheimer amyloid-beta protein
1047 induce reversible synapse loss by modulating an NMDA-type glutamate receptor-
1048 dependent signaling pathway. *J Neurosci*, 27(11), 2866-2875.
1049 <https://doi.org/10.1523/JNEUROSCI.4970-06.2007>
- 1050
- 1051 Shankar, G. M., Li, S., Mehta, T. H., Garcia-Munoz, A., Shepardson, N. E., Smith, I.,
1052 Brett, F. M., Farrell, M. A., Rowan, M. J., Lemere, C. A., Regan, C. M., Walsh, D.
1053 M., Sabatini, B. L., & Selkoe, D. J. (2008). Amyloid-beta protein dimers isolated
1054 directly from Alzheimer's brains impair synaptic plasticity and memory. *Nat Med*,
1055 14(8), 837-842. <https://doi.org/10.1038/nm1782>
- 1056
- 1057 Shoji, M., Golde, T. E., Ghiso, J., Cheung, T. T., Estus, S., Shaffer, L. M., Cai, X. D.,
1058 McKay, D. M., Tintner, R., Frangione, B., & et al. (1992). Production of the
1059 Alzheimer amyloid beta protein by normal proteolytic processing. *Science*,
1060 258(5079), 126-129. <https://doi.org/10.1126/science.1439760>
- 1061
- 1062 Sinnen, B. L., Bowen, A. B., Gibson, E. S., & Kennedy, M. J. (2016). Local and Use-
1063 Dependent Effects of beta-Amyloid Oligomers on NMDA Receptor Function
1064 Revealed by Optical Quantal Analysis. *J Neurosci*, 36(45), 11532-11543.
1065 <https://doi.org/10.1523/JNEUROSCI.1603-16.2016>
- 1066
- 1067 Smith, K. R., Kopeikina, K. J., Fawcett-Patel, J. M., Leaderbrand, K., Gao, R.,
1068 Schurmann, B., Myczek, K., Radulovic, J., Swanson, G. T., & Penzes, P. (2014).
1069 Psychiatric risk factor ANK3/ankyrin-G nanodomains regulate the structure and
1070 function of glutamatergic synapses. *Neuron*, 84(2), 399-415.
1071 <https://doi.org/10.1016/j.neuron.2014.10.010>
- 1072
- 1073 Sugiura, Y., Ikeda, K., & Nakano, M. (2015). High Membrane Curvature Enhances
1074 Binding, Conformational Changes, and Fibrillation of Amyloid-beta on Lipid
1075 Bilayer Surfaces. *Langmuir*, 31(42), 11549-11557.
1076 <https://doi.org/10.1021/acs.langmuir.5b03332>
- 1077
- 1078 Takahashi, R. H., Almeida, C. G., Kearney, P. F., Yu, F., Lin, M. T., Milner, T. A., &
1079 Gouras, G. K. (2004). Oligomerization of Alzheimer's beta-amyloid within
1080 processes and synapses of cultured neurons and brain. *J Neurosci*, 24(14),
1081 3592-3599. <https://doi.org/10.1523/JNEUROSCI.5167-03.2004>
- 1082

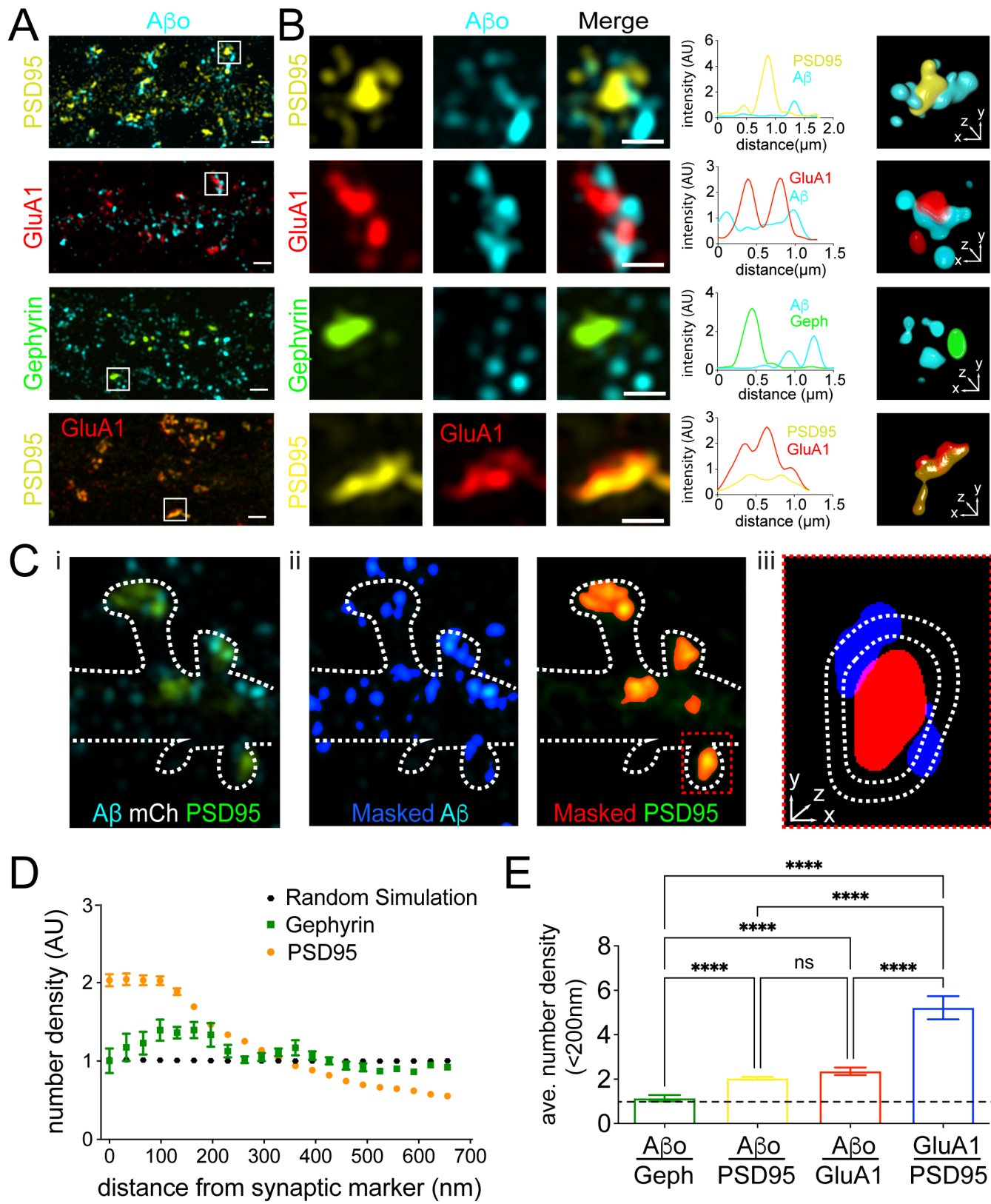
- 1083 Takahashi, R. H., Milner, T. A., Li, F., Nam, E. E., Edgar, M. A., Yamaguchi, H., Beal,
1084 M. F., Xu, H., Greengard, P., & Gouras, G. K. (2002). Intraneuronal Alzheimer
1085 A β 42 Accumulates in Multivesicular Bodies and Is Associated with Synaptic
1086 Pathology. *The American Journal of Pathology*, 161(5), 1869-1879.
1087 [https://doi.org/10.1016/s0002-9440\(10\)64463-x](https://doi.org/10.1016/s0002-9440(10)64463-x)
- 1088
- 1089 Tang, A. H., Chen, H., Li, T. P., Metzbower, S. R., MacGillavry, H. D., & Blanpied, T. A.
1090 (2016). A trans-synaptic nanocolumn aligns neurotransmitter release to
1091 receptors. *Nature*, 536(7615), 210-214. <https://doi.org/10.1038/nature19058>
- 1092
- 1093 Terakawa, M. S., Lin, Y., Kinoshita, M., Kanemura, S., Itoh, D., Sugiki, T., Okumura, M.,
1094 Ramamoorthy, A., & Lee, Y. H. (2018). Impact of membrane curvature on
1095 amyloid aggregation. *Biochim Biophys Acta Biomembr*, 1860(9), 1741-1764.
1096 <https://doi.org/10.1016/j.bbamem.2018.04.012>
- 1097
- 1098 Terry, R. D., Masliah, E., Salmon, D. P., Butters, N., DeTeresa, R., Hill, R., Hansen, L.
1099 A., & Katzman, R. (1991). Physical basis of cognitive alterations in Alzheimer's
1100 disease: synapse loss is the major correlate of cognitive impairment. *Ann Neurol*,
1101 30(4), 572-580. <https://doi.org/10.1002/ana.410300410>
- 1102
- 1103 Texido, L., Martin-Satue, M., Alberdi, E., Solsona, C., & Matute, C. (2011). Amyloid beta
1104 peptide oligomers directly activate NMDA receptors. *Cell Calcium*, 49(3), 184-
1105 190. <https://doi.org/10.1016/j.ceca.2011.02.001>
- 1106
- 1107 Um, J. W., Kaufman, A. C., Kostylev, M., Heiss, J. K., Stagi, M., Takahashi, H., Kerrisk,
1108 M. E., Vortmeyer, A., Wisniewski, T., Koleske, A. J., Gunther, E. C., Nygaard, H.
1109 B., & Strittmatter, S. M. (2013). Metabotropic glutamate receptor 5 is a
1110 coreceptor for Alzheimer abeta oligomer bound to cellular prion protein. *Neuron*,
1111 79(5), 887-902. <https://doi.org/10.1016/j.neuron.2013.06.036>
- 1112
- 1113 Um, J. W., Nygaard, H. B., Heiss, J. K., Kostylev, M. A., Stagi, M., Vortmeyer, A.,
1114 Wisniewski, T., Gunther, E. C., & Strittmatter, S. M. (2012). Alzheimer amyloid-
1115 beta oligomer bound to postsynaptic prion protein activates Fyn to impair
1116 neurons. *Nat Neurosci*, 15(9), 1227-1235. <https://doi.org/10.1038/nn.3178>
- 1117
- 1118 Walsh, D. M., Klyubin, I., Fadeeva, J. V., Cullen, W. K., Anwyl, R., Wolfe, M. S., Rowan,
1119 M. J., Selkoe, D. J. (2002). Naturally secreted oligomers of amyloid b protein
1120 potently inhibit hippocampal long-term potentiation *in-vivo letters to nature*, 416,
1121 535-539.
- 1122
- 1123 Wang, Y., Schnitzbauer, J., Hu, Z., Li, X., Cheng, Y., Huang, Z. L., & Huang, B. (2014).
1124 Localization events-based sample drift correction for localization microscopy with
1125 redundant cross-correlation algorithm. *Opt Express*, 22(13), 15982-15991.
1126 <https://doi.org/10.1364/OE.22.015982>
- 1127

- 1128 Wei, W., Nguyen, L. N., Kessels, H. W., Hagiwara, H., Sisodia, S., & Malinow, R.
1129 (2010). Amyloid beta from axons and dendrites reduces local spine number and
1130 plasticity. *Nat Neurosci*, 13(2), 190-196. <https://doi.org/10.1038/nn.2476>
- 1131
- 1132 Zhang, C., Kang, J. S., Asano, S. M., Gao, R., & Boyden, E. S. (2020). Expansion
1133 Microscopy for Beginners: Visualizing Microtubules in Expanded Cultured HeLa
1134 Cells. *Curr Protoc Neurosci*, 92(1), e96. <https://doi.org/10.1002/cpns.96>
- 1135
- 1136 Zhao, W. Q., Santini, F., Breese, R., Ross, D., Zhang, X. D., Stone, D. J., Ferrer, M.,
1137 Townsend, M., Wolfe, A. L., Seager, M. A., Kinney, G. G., Shughrue, P. J., &
1138 Ray, W. J. (2010). Inhibition of calcineurin-mediated endocytosis and alpha-
1139 amino-3-hydroxy-5-methyl-4-isoxazolepropionic acid (AMPA) receptors prevents
1140 amyloid beta oligomer-induced synaptic disruption. *J Biol Chem*, 285(10), 7619-
1141 7632. <https://doi.org/10.1074/jbc.M109.057182>
- 1142
- 1143
- 1144
- 1145

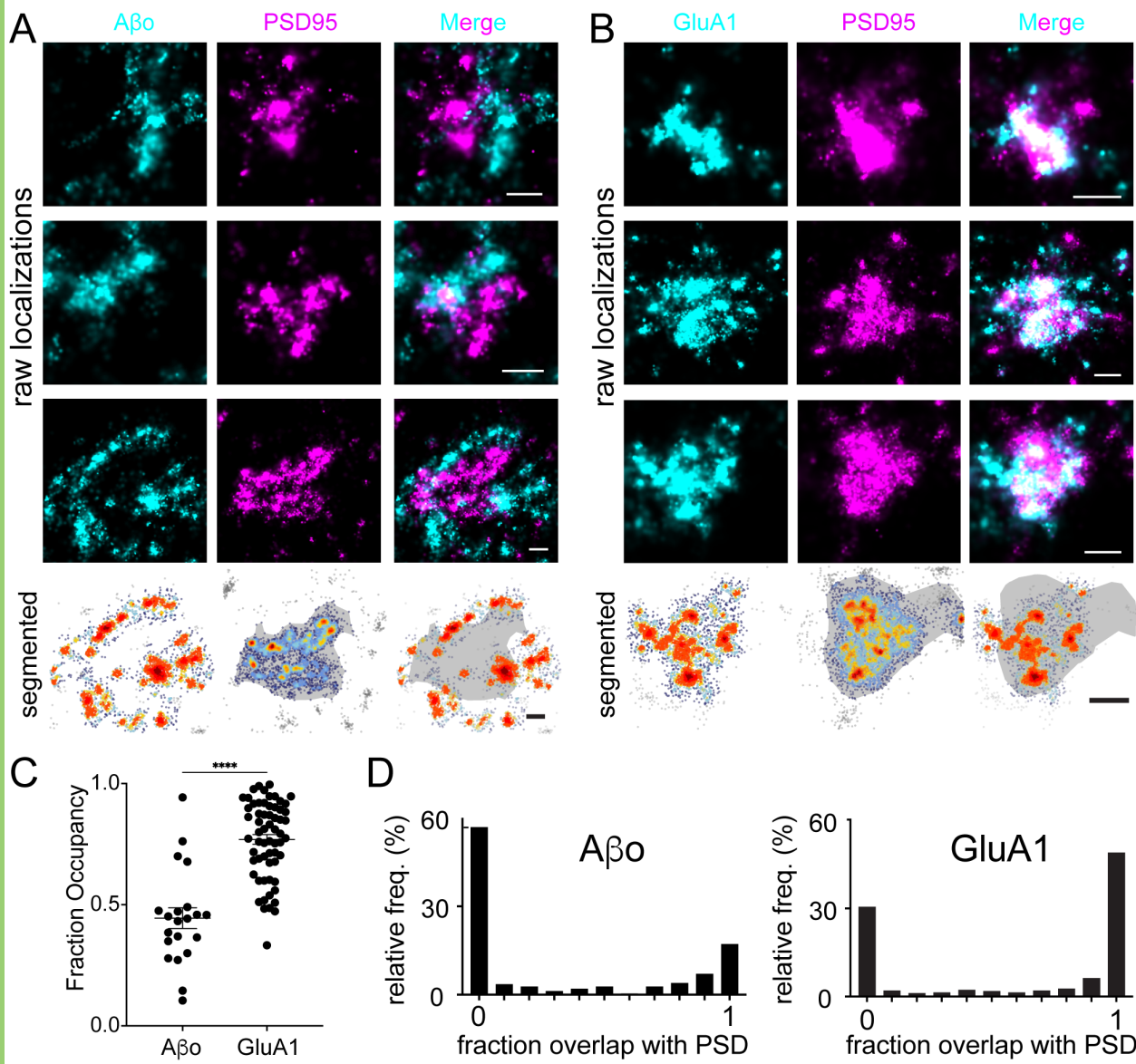
Actor-Engel et. al Figure 1



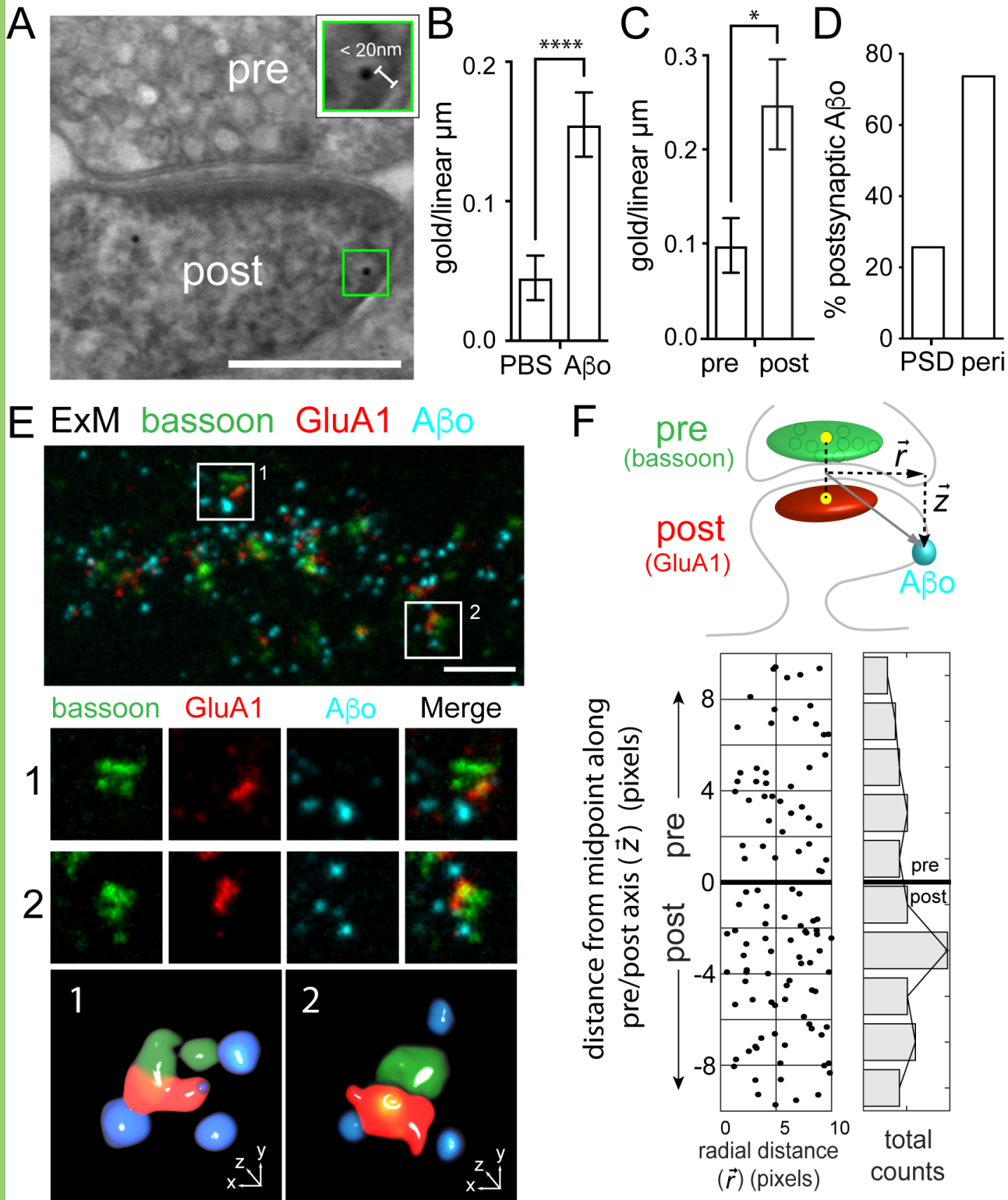
Actor-Engel et. al Figure 2



Actor-Engel et. al Figure 3



Actor-Engel et. al Figure 4



Actor-Engel et al., Figure 5

